DE GRUYTER

Russ. J. Numer. Anal. Math. Modelling 2021; 36(3):165–176

Kirill Nikitin, Yuri Vassilevski, and Ruslan Yanbarisov*

An implicit scheme for simulation of free surface non-Newtonian fluid flows on dynamically adapted grids

Abstract: This work presents a new approach to modelling of free surface non-Newtonian (viscoplastic or viscoelastic) fluid flows on dynamically adapted octree grids. The numerical model is based on the implicit formulation and the staggered location of governing variables. We verify our model by comparing simulations with experimental and numerical results known from the literature.

Free surface flows of viscoplastic and viscoelastic fluids are common in nature and have a wide range of applications in engineering. Viscoelasticity plays a big role in polymer processing such as extrudate swelling [13, 22] and melt fracture [9, 14] phenomena seen in extrusion. Viscoplastic fluid flows span lava flows, snow avalanches, debris flows, flows of molten metal, fresh concrete, pastes and other concentrated suspensions in engineering applications. Although the rheology of such materials may be quite complicated, viscoplastic models based on the strain rate-stress tensor relationship can predict dynamics of such fluids with reasonable accuracy [8, 11].

This work considers the Herschel–Bulkley viscoplastic and Oldroyd-B viscoelastic fluid models. Each model is regarded as the popular option for simulations of plastic and elastic effects. In particular, Oldroyd-B fluid model is extensively used for benchmarking of numerical models [1, 2, 15, 24].

Our first numerical model of free surface viscoplastic fluid flow verified on experimental data, was suggested in [16]. The time discretization was based on the projection scheme for the Navier–Stokes equation and the spatial discretization exploited a hybrid finite volume / finite difference method on adaptive octree hexahedral grids [17, 20]. The discretization in space included high order interpolation with a limiting strategy for semi-Lagrangian transport of the free surface (for details we refer to [18, 23]).

The novelty of the present work is the extension of the existing incompressible viscous fluid flow solver to the viscoelastic case and handling its fluid dynamics step implicitly which provides robust simulations for both viscoelastic and viscoplastic fluids flows.

The article is organized as follows. In Section 1 we consider the governing equations for free surface non-Newtonian fluid flows in terms of Herschel–Bulkley and Oldroyd-B models. In Section 2 we introduce the numerical method for the approximate solution of the presented equations including the time integration and the spatial discretization details. We briefly sketch the discretization techniques of the existing method and focus on the discretization of new elastic terms. In Section 3 we verify the method on numerical and experimental data presented in the literature.

Kirill Nikitin, Marchuk Institute of Numerical Mathematics RAS, Moscow 119333, Russia
Yuri Vassilevski, Marchuk Institute of Numerical Mathematics RAS, Moscow 119333, Russia; Sechenov University, Moscow 119991, Russia; Moscow Institute of Physics and Technology, Dolgoprudny 141701, Moscow Region, Russia
*Corresponding author: Ruslan Yanbarisov, Marchuk Institute of Numerical Mathematics RAS, Moscow 119333, Russia; Sechenov University, Moscow 119991, Russia. E-mail: ruslan.yanbarisov@gmail.com

1 Governing equations

1.1 General setting

We consider flow of free surface incompressible fluid in a bounded time-dependent domain $\Omega(t) \in \mathbb{R}^3$, $t \in (0, T]$. The boundary $\partial\Omega(t)$ is assumed to be split into a static part Γ_D representing walls and a free surface $\Gamma(t)$.

The momentum and mass conservation equations for incompressible flows are:

$$\rho\left(\frac{\partial \mathbf{u}}{\partial t} + (\mathbf{u} \cdot \nabla)\mathbf{u}\right) = -\nabla p + \nabla \cdot \boldsymbol{\tau} + \rho\mathbf{g} \quad \text{in} \quad \Omega(t) \tag{1.1}$$

$$\nabla \cdot \mathbf{u} = 0$$

where $\mathbf{u} = (u, v, w)^T$ is the velocity vector, p is the scalar pressure, ρ is the constant fluid density, $\mathbf{g}$ is the gravity acceleration vector, and $\boldsymbol{\tau}$ is the deviatoric part of the stress tensor.

At the initial time $t = 0$ the domain and velocity field are known:

$$\Omega(0) = \Omega^0, \quad \mathbf{u}|_{t=0} = \mathbf{u}^0. \tag{1.2}$$

On the static boundary we assume that the velocity field satisfies the Dirichlet boundary condition

$$\mathbf{u} = \mathbf{u}_D \quad \text{on } \Gamma_D \tag{1.3}$$

where $\mathbf{u}_D$ is given. On the free surface $\Gamma(t)$ we impose the kinematic condition

$$v_\Gamma = \mathbf{u}|_\Gamma \cdot \mathbf{n}_\Gamma \tag{1.4}$$

where $\mathbf{n}_\Gamma$ is the outer normal vector for $\Gamma(t)$ and v_Γ is the normal velocity of the free surface $\Gamma(t)$. The surface tension and the normal fluid stresses are balanced on the free surface $\Gamma(t)$:

$$-p\mathbf{n}_\Gamma + \boldsymbol{\tau}\mathbf{n}_\Gamma = \zeta\varkappa\mathbf{n}_\Gamma - p_{\text{ext}}\mathbf{n}_\Gamma \quad \text{on } \Gamma(t) \tag{1.5}$$

where $\varkappa$ is the sum of the principal curvatures, ζ is the surface tension coefficient, p_{ext} is the exterior pressure which we assume to be zero, $p_{\text{ext}} = 0$.

In order to track the free surface position, we use the implicit definition of $\Gamma(t)$ via the zero level isosurface of a globally defined level set function $\varphi(t, \mathbf{x})$ [21]:

$$\varphi(t, \mathbf{x}) \begin{cases} < 0, & \mathbf{x} \in \Omega(t) \\ > 0, & \mathbf{x} \in \mathbb{R}^3 \setminus \overline{\Omega(t)} \\ = 0, & \mathbf{x} \in \Gamma(t) \end{cases} \quad \forall t \in [0, T].$$

The initial condition (1.2) determines $\varphi^0 = \varphi(0, \mathbf{x})$. At any time $t > 0$, the level set function φ satisfies the transport equation:

$$\frac{\partial \varphi}{\partial t} + \tilde{\mathbf{u}} \cdot \nabla\varphi = 0 \quad \text{in } \mathbb{R}^3 \times (0, T] \tag{1.6}$$

where $\tilde{\mathbf{u}}$ is the fluid velocity field extended outside $\Omega(t)$. It is common to require the signed distance property of φ in terms of the Eikonal equation:

$$|\nabla\varphi| = 1. \tag{1.7}$$

Apart of the boundary position, the level set function φ provides the outer normal $\mathbf{n}_\Gamma = \nabla\varphi/|\nabla\varphi|$ and the curvature of the free surface $\varkappa = \nabla \cdot \mathbf{n}_\Gamma$.

The fluid rheology is governed by the constitutive law for the deviatoric part of the stress tensor $\boldsymbol{\tau}$. We describe viscoplastic and viscoelastic fluid models in terms of dependence of $\boldsymbol{\tau}$ on the strain rate tensor $\mathbf{D} = \frac{1}{2}[\nabla\mathbf{u} + (\nabla\mathbf{u})^T]$.

1.2 Viscoplastic fluid

We address viscoplastic fluids described by the Herschel–Bulkley constitutive law:

$$\boldsymbol{\tau} = \left(K|\mathbf{D}|^{n-1} + \tau_s|\mathbf{D}|^{-1} \right)\mathbf{D} \;\leftrightarrow\; |\boldsymbol{\tau}| > \tau_s \tag{1.8}$$

$$\mathbf{D} = \mathbf{0} \;\leftrightarrow\; |\boldsymbol{\tau}| \leqslant \tau_s \tag{1.9}$$

where $|\mathbf{D}| = \left(2 \sum_{1 \leqslant i,j \leqslant 3} \mathbf{D}_{ij}^2\right)^{1/2}$ is the shear rate, K is the consistency parameter, τ_s is the yield stress, n is the flow index (for $n < 1$ the fluid exhibits shear-thinning property, for $n > 1$ it is shear-thickening; $n = 1$ corresponds to the Bingham plastic). The yield stress τ_s controls the transition between flow region (1.8) and plug region (1.9).

Since the stress tensor is not determined in the plug region, we regularize the plasticity term by the Bercovier–Engelman method [3] and replace $|\mathbf{D}|^{-1}$ by $|\mathbf{D}|_\varepsilon^{-1} = \left(|\mathbf{D}|^2 + \varepsilon^2\right)^{-1/2}$ with a small $\varepsilon > 0$ in (1.8), (1.9).

The regularization allows us to pose equations in the entire fluid domain:

$$\rho\left(\frac{\partial \mathbf{u}}{\partial t} + (\mathbf{u} \cdot \nabla)\mathbf{u}\right) = -\nabla p + \nabla \cdot (\mu_\varepsilon \mathbf{D}) + \rho \mathbf{g} \quad \text{in} \quad \Omega(t) \tag{1.10}$$
$$\nabla \cdot \mathbf{u} = 0$$

with the shear-dependent effective viscosity

$$\mu_\varepsilon = K|\mathbf{D}|_\varepsilon^{n-1} + \tau_s|\mathbf{D}|_\varepsilon^{-1}. \tag{1.11}$$

1.3 Viscoelastic fluid

We consider viscoelastic fluids described by the Oldroyd-B model:

$$\boldsymbol{\tau} + \lambda_1 \overset{\triangledown}{\boldsymbol{\tau}} = 2\mu_0\left(\mathbf{D} + \lambda_2 \overset{\triangledown}{\mathbf{D}}\right) \tag{1.12}$$

where λ_1 is the relaxation time, $\lambda_2 \leqslant \lambda_1$ is the retardation time, μ_0 is the total viscosity of the fluid. The upper-convected derivative $\overset{\triangledown}{\mathbf{C}}$ for a tensor $\mathbf{C}$ given by

$$\overset{\triangledown}{\mathbf{C}} = \frac{\partial \mathbf{C}}{\partial t} + (\mathbf{u} \cdot \nabla)\,\mathbf{C} - (\nabla \mathbf{u})^T\mathbf{C} - \mathbf{C}(\nabla \mathbf{u}) \tag{1.13}$$

represents transport, rotation, and dilation of the tensor.

We introduce the retardation parameter $\beta = \lambda_2/\lambda_1$, define the Newtonian viscosity $\mu_S = \beta\mu_0$ and split the stress tensor into elastic and viscous parts [24]:

$$\boldsymbol{\tau} = \boldsymbol{\tau}_P + 2\mu_S\mathbf{D} \tag{1.14}$$

where $\boldsymbol{\tau}_P$ is the elastic stress tensor. The coefficient $\beta \leqslant 1$ measures the ratio between the Newtonian and the total viscosity of the fluid. When $\beta = 1$, the model describes the Newtonian flow.

Substitution of (1.14) into (1.12) allows us to eliminate $\overset{\triangledown}{\mathbf{D}}$ and derive the equation for the elastic stress tensor $\boldsymbol{\tau}_P$:

$$\boldsymbol{\tau}_P + \lambda_1 \overset{\triangledown}{\boldsymbol{\tau}}_P = 2(1 - \beta)\mu_0\mathbf{D}. \tag{1.15}$$

Next, we introduce the conformation tensor $\mathbf{A}$ represented by a symmetric positive-definite 3×3 matrix. The conformation tensor is the internal variable describing the macromolecular configuration of polymer chains and defining the elastic stress tensor

$$\boldsymbol{\tau}_P = \frac{\mu_0}{\lambda_1}(1 - \beta)(\mathbf{A} - \mathbf{I}). \tag{1.16}$$

Combination of (1.13), (1.15), (1.16) yields the following time evolution equation for the conformation tensor:

$$\mathbf{A} + \lambda_1 \overset{\triangledown}{\mathbf{A}} = \mathbf{I}. \tag{1.17}$$

Finally, the governing equations for the Oldroyd-B fluid in terms of unknown $\mathbf{u}$, p, $\mathbf{A}$ are:

$$\rho \left(\frac{\partial \mathbf{u}}{\partial t} + (\mathbf{u} \cdot \nabla)\mathbf{u} \right) - \beta\mu_0 \Delta\mathbf{u} - \mu_0\lambda_1^{-1}(1 - \beta)\nabla \cdot \mathbf{A} = -\nabla p + \rho\mathbf{g}$$

$$\mathbf{A} + \lambda_1 \overset{\triangledown}{\mathbf{A}} = \mathbf{I}$$

$$\nabla \cdot \mathbf{u} = 0. \tag{1.18}$$

For the initial conditions we assume that no elastic deformations are present in the fluid and thus

$$\mathbf{A}|_{t=0} = \mathbf{I}. \tag{1.19}$$

The conformation tensor should satisfy the following boundary conditions. On the static boundary Γ_D we impose the homogeneous Neumann boundary condition $\partial\mathbf{A}/\partial\mathbf{n} = 0$. On the free surface we impose the zero traction boundary condition (1.5):

$$2\mu_S \mathbf{D}\mathbf{n}_\Gamma + \mu_0\lambda_1^{-1}(1 - \beta)(\mathbf{A} - \mathbf{I})\mathbf{n}_\Gamma + p\mathbf{n}_\Gamma = \zeta\varkappa\mathbf{n}_\Gamma. \tag{1.20}$$

2 Numerical method

The numerical method for the approximate solution of (1.6), (1.10) or (1.6), (1.18) is based on the approach developed in our previous works for the Newtonian [17, 18, 20] and viscoplastic [16] flows.

We adopt the notation $\mathbf{u}^n$, p^n, φ^n, $\mathbf{A}^n$ for approximations to the velocity field, the pressure, the level set function and the conformation tensor at $t = t^n$, respectively. The initial conditions (1.2) provide $\mathbf{u}^0$ and φ^0. The level set function φ^n implicitly defines an approximation to fluid domain at time $t = t^n$ through $\Omega^n = \mathbf{x} \in \mathbb{R}^3 : \varphi^n(\mathbf{x}) < 0$.

Given $\mathbf{u}^n$, p^n, φ^n, and optionally $\mathbf{A}^n$, the free surface flow solver performs two major substeps at time step t^{n+1}:

– Find the new level set function φ^{n+1} and the fluid domain Ω^{n+1};
– Solve (1.1) in Ω^{n+1} fully implicitly to find $\mathbf{u}^{n+1}$, p^{n+1}, and optionally $\mathbf{A}^{n+1}$.

These substeps are discussed in the following sections. The computational mesh is assumed to be an octree grid in a bounding cube admitting refinement and derefinement.

2.1 Free surface update

Given $\mathbf{u}^n$ and φ^n such that $\nabla \cdot \mathbf{u}^n = 0$, $|\nabla\varphi^n| = 1$, we find φ^{n+1} as follows:

(1) Mesh adaptation. Refine the computational mesh according to the *predicted* position of the zero level set $\widetilde{\varphi}^{n+1}$.
(2) Surface advection. Solve (1.6) by a semi-Lagrangian BFECC method with tricubic limited interpolation [18, 23] to get the new level set φ_d^{n+1}. Mesh refinement at the previous step is crucial for large time steps since the advected fluid boundary may pass through coarse cells which will result in a severe loss of accuracy.
(3) Volume correction. Update the level set function $\varphi^{n+1} = \varphi_d^{n+1} + \eta$, where η solves the volume conservation equation $|V(\varphi_d^{n+1} + \eta) - V(\varphi^n)| = 0$. Set Ω^{n+1} by $\varphi^{n+1}(x) < 0$ and Γ^{n+1} by $\varphi^{n+1}(x) = 0$. For details of an advanced volume correction scheme we refer to [19].
(4) Remeshing. Locally update the octree mesh by adapting it to Γ^{n+1} via refinement and derefinement of mesh cells.

(5) Re-interpolation. Map all discrete variables to the new grid using the simplest interpolation [20].

(6) Re-initialization. Update the level set function φ^{n+1} to satisfy the Eikonal equation (1.7) and perform the volume correction once again [19].

At the end of the free surface update we have φ^{n+1}, Ω^{n+1} as well as geometric features of Γ^{n+1} such as the outer normal $\mathbf{n}_\Gamma^{n+1}$ and the sum of the principal curvatures $\varkappa^{n+1}$.

2.2 Implicit scheme for the fluid flow

The linearized semi-discrete system for (1.1) can be written in the general form:

$$\rho\left(\left[\frac{\partial \mathbf{u}}{\partial t}\right]^{n+1} + \left(\widetilde{\mathbf{u}^{n+1}} \cdot \nabla\right)\mathbf{u}^{n+1}\right) - \nabla \cdot \widehat{\boldsymbol{\tau}}^{n+1} + \nabla p^{n+1} = \rho\mathbf{g} \tag{2.1}$$

$$\nabla \cdot \mathbf{u}^{n+1} = 0 \tag{2.2}$$

with the extrapolated velocity $\widetilde{\mathbf{u}^{n+1}} = \mathbf{u}^n + \xi(\mathbf{u}^n - \mathbf{u}^{n-1})$, where $\xi = \Delta t^n/\Delta t^{n-1}$.

In the case of viscoplastic fluid the deviatoric stress is linearized:

$$\widehat{\boldsymbol{\tau}}^{n+1} = 2\mu_\varepsilon(\widetilde{\mathbf{D}^{n+1}})\mathbf{D}^{n+1}.$$

where $\mu_\varepsilon(\cdot)$ is the shear-dependent effective viscosity (1.11), and $\widetilde{\mathbf{D}^{n+1}}$ is the strain rate tensor for $\widetilde{\mathbf{u}^{n+1}}$.

In the case of viscoelastic fluid the deviatoric stress $\widehat{\boldsymbol{\tau}}^{n+1} = \beta\mu_0\mathbf{D}^{n+1} + \frac{\mu_0}{\lambda_1}(1-\beta)(\mathbf{A}^{n+1} - \mathbf{I})$ depends on $\mathbf{A}^{n+1}$ satisfying the evolution equation

$$\mathbf{A}^{n+1} + \lambda_1\left(\left[\frac{\partial \mathbf{A}}{\partial t}\right]^{n+1} + \left(\widetilde{\mathbf{u}^{n+1}} \cdot \nabla\right)\mathbf{A}^{n+1} - (\nabla\mathbf{u}^n)^T\mathbf{A}^{n+1} - \mathbf{A}^{n+1}(\nabla\mathbf{u}^n)\right) = \mathbf{I}. \tag{2.3}$$

The time derivative is discretized by the BDF2 formula at time t^{n+1}:

$$\left[\frac{\partial \mathbf{u}}{\partial t}\right]^{n+1} = \frac{\alpha_1\mathbf{u}^{n+1} + \alpha_2\mathbf{u}^n + \alpha_3\mathbf{u}^{n-1}}{\Delta t^n}, \quad \alpha_1 = \frac{2\xi + 1}{\xi + 1}, \quad \alpha_2 = -\frac{\xi^2 + 2\xi + 1}{\xi + 1}, \quad \alpha_3 = \frac{\xi^2}{\xi + 1}. \tag{2.4}$$

The equations (2.1)–(2.2) are discretized in space on staggered octree grids by the hybrid finite volume/finite difference method [20]. The pressure degrees of freedom are assigned to centers of cells, the velocity components are collocated at cell faces in such a way that every face stores the normal velocity component, and the conformation tensor components are collocated at cell vertices. Since the conformation tensor is a symmetric 3×3 matrix, we store its six components per each node.

The finite volume discretization of the inertia and diffusion terms is based on a control volume V' associated to each cell face F (see [20] for more details). The linearized conservative form of the inertia terms $(\widetilde{\mathbf{u}^{n+1}} \cdot \nabla)\mathbf{u}^{n+1} = \nabla \cdot (\mathbf{u}^{n+1}\widetilde{\mathbf{u}^{n+1}})$ is used in the finite volume discretization. For instance, the x-component of the velocity inertia term is:

$$\nabla \cdot (u^{n+1}\widetilde{\mathbf{u}^{n+1}})(\mathbf{x}_F) \approx |V'|^{-1} \sum_{F' \in \mathcal{F}(V')} |F'|(\widetilde{\mathbf{u}^{n+1}} \cdot \mathbf{n})(\mathbf{x}_{F'})u^{n+1}(\mathbf{x}_{F'})$$

where $\mathcal{F}(V')$ is the set of the control volume faces, $\mathbf{x}_{F'}$ denotes the barycenter of face F', $\mathbf{n}$ denotes the unit outer normal to the face. The advection fluxes $(\widetilde{\mathbf{u}^{n+1}} \cdot \mathbf{n})u^{n+1}$ are discretized by the third order upwind discretization which uses the fan triangulation interpolation for missing values [20].

In the finite volume discretization of the viscous terms we use the face control volume V' as well:

$$\nabla \cdot \left(\mu\nabla u^{n+1}\right)(\mathbf{x}_F) \approx |V'|^{-1} \sum_{F' \in \mathcal{F}(V')} |F'|(\mu\nabla_h u \cdot \mathbf{n})(\mathbf{x}_{F'})$$

where $\mu = \mu_\varepsilon(\widetilde{\mathbf{D}^{n+1}})$ is the precomputed effective viscosity of the viscoplastic fluid, or $\mu = \beta\mu_0 = \text{const}$ is the Newtonian viscosity of the viscoelastic fluid. The viscous flux $\mu\nabla_h u \cdot \mathbf{n}$ is computed by the third order finite difference discretization [20].
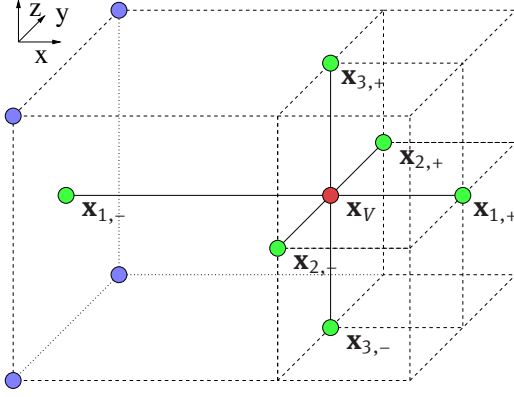
Fig. 1: Discretization stencil (green) for the first partial derivatives at an octree node $\mathbf{x}_V$ (red). The missing value at $\mathbf{x}_{1,-}$ is interpolated from available nodal values (blue).

The finite volume discretization of the incompressibility equation (2.2) on each octree cell V with faces $\mathcal{F}(V)$ is evident:

$$|V|^{-1} \sum_{F \in \mathcal{F}(V)} |F|(\mathbf{n} \cdot \mathbf{u}^{n+1})(\mathbf{x}_F) = 0. \tag{2.5}$$

Thanks to the staggered location of the velocity components, the fluxes $(\mathbf{u}^{n+1} \cdot \mathbf{n})(\mathbf{x}_F)$ are easily computed.

The pressure gradient term in (2.1) is discretized by the finite difference method based on the formal Taylor expansion (see [18]).

The discretization of the elastic term as well as the conformation tensor evolution equation are considered in the next section.

2.3 Handling the conformation tensor

The conformation tensor $\mathbf{A}$ contributes to (2.1), (2.3) via the advection term $(\widetilde{\mathbf{u}^{n+1}} \cdot \nabla)\mathbf{A}$, the rotation/dilation term $(\nabla \mathbf{u}^n)^T \mathbf{A} - \mathbf{A}(\nabla \mathbf{u}^n)$, and the vector divergence term

$$\nabla \cdot \mathbf{A} = \begin{bmatrix} \dfrac{\partial A_{xx}}{\partial x} + \dfrac{\partial A_{xy}}{\partial y} + \dfrac{\partial A_{xz}}{\partial z} \\ \dfrac{\partial A_{xy}}{\partial x} + \dfrac{\partial A_{yy}}{\partial y} + \dfrac{\partial A_{yz}}{\partial z} \\ \dfrac{\partial A_{xz}}{\partial x} + \dfrac{\partial A_{yz}}{\partial y} + \dfrac{\partial A_{zz}}{\partial z} \end{bmatrix}. \tag{2.6}$$

The x-, y-, and z-components of the latter should be discretized at centers of x-, y-, and z-orthogonal faces of each octree cell, respectively. To this end, we first discretize the partial derivatives at the nodes of the octree mesh, and then average the discretizations to the face centers. The partial derivatives at the octree nodes are approximated by the second order finite difference. If the stencil misses a collocated value, the latter is interpolated from neighboring nodal values. For example, in notations of Fig. 1, we have

$$\frac{\partial A_{xy}}{\partial x}(\mathbf{x}_V) \approx \frac{r}{(h+r)h} A_{xy}(\mathbf{x}_{1,+}) + \frac{h-r}{hr} A_{xy}(\mathbf{x}_V) - \frac{h}{(h+r)r} A_{xy}(\mathbf{x}_{1,-}) \tag{2.7}$$

where $h = |\mathbf{x}_{1,+} - \mathbf{x}_V|$, $r = |\mathbf{x}_{1,-} - \mathbf{x}_V|$.

The advection term $(\widetilde{\mathbf{u}^{n+1}} \cdot \nabla)\mathbf{A}$ is discretized at centers of x-, y-, z-orthogonal faces of each octree cell in the similar way.

The rotation/dilation term $\mathbf{M}$ may be rewritten via the strain rate tensor $\mathbf{D}$ and the vorticity tensor $\mathbf{W} = \frac{1}{2}(\nabla \mathbf{u} - \nabla \mathbf{u}^T)$:

$$\mathbf{M} = (\nabla \mathbf{u})^T \mathbf{A} + \mathbf{A}(\nabla \mathbf{u}) = \mathbf{W}\mathbf{A} - \mathbf{A}\mathbf{W} + (\mathbf{A}\mathbf{D} + \mathbf{D}\mathbf{A})$$

which motivates its name. The six independent components of the symmetric rotation/dilation tensor **M** are

$$
\begin{bmatrix}
M_{xx} \\
M_{yy} \\
M_{zz} \\
M_{xy} \\
M_{xz} \\
M_{yz}
\end{bmatrix}
=
\begin{bmatrix}
2u_x A_{xx} + (u_y + v_x) A_{xy} + (u_z + w_x) A_{xz} \\
(u_y + v_x) A_{xy} + 2v_y A_{yy} + (v_z + w_y) A_{yz} \\
(w_x + u_z) A_{xz} + (w_y + v_z) A_{yz} + 2w_z A_{zz} \\
(u_x + v_y) A_{xy} + v_x (A_{xx} + A_{yy}) + v_z A_{xz} + w_x A_{yz} \\
(u_x + w_z) A_{xz} + w_x (A_{xx} + A_{zz}) + v_x A_{yz} + w_y A_{xy} \\
(v_y + w_z) A_{yz} + w_y (A_{yy} + A_{zz}) + u_y A_{xz} + w_x A_{xy}
\end{bmatrix}.
\tag{2.8}
$$

The partial derivatives u_x, v_y, w_z are approximated at an octree node $\mathbf{x}_V$ by the least-squares fitting of respective central finite differences at neighboring octree cells centers $u_x^h(\mathbf{x}_{c_i})$, $v_y^h(\mathbf{x}_{c_i})$, $w_z^h(\mathbf{x}_{c_i})$. Any other velocity component partial derivative (e.g. u_y) is discretized at an octree node $\mathbf{x}_V$ as the directional derivative of a linear 2D function defined in the plane orthogonal to the considered component (e.g. yz-plane). The function is fitted by the least squares to values at the closest points (cell centers or cell faces centers) surrounding $\mathbf{x}_V$. The latter values for the velocity component are either known (at cell faces centers) or are interpolated from two known values (at cell centers).

3 Verification and validation of the numerical models

In this section we validate the presented framework for free surface viscoplastic and viscoelastic fluid flow modelling. The first benchmark addresses impact of a viscoelastic Oldroyd-B drop on a solid floor [24, 25]. The next benchmark is focused on oscillating droplets of Bingham [6, 16] and Oldroyd-B fluids. The last benchmark concerns break of a dam on an inclined surface and filled with viscoplastic Herschel–Bulkley fluid [7].

3.1 Drop impacting

To verify our viscoelastic model, we simulate falling of a spherical drop of Oldroyd-B fluid on a floor [24, 25].

The test setup is shown in Fig. 2: an initially spherical drop of diameter d_0 falls from height H to a rigid surface. At the beginning of the simulation, the drop starts to fall in the gravity field with the initial velocity $w = -U$ directed towards the floor. We neglect the surface tension forces and the stress tensor $\boldsymbol{\tau}$ is initially set to zero. After the droplet hits the surface, it is supposed to flow radially increasing its diameter $d(t)$ until the elastic forces come into play, reversing the velocities and causing the droplet to contract back.

First, we compare the behaviour of the Newtonian fluid in our simulation with numerical simulations obtained by other researchers. The viscosity, density as well as other parameters of the problem are listed in Table 1. Simulations terminate at the dimensionless time $t(U/d_0) = 5$. Two dynamically adapted octree meshes are used in the simulations: M1 mesh has $h_{\min} = d_0/32$, $h_{\max} = d_0/16$, and M2 mesh has $h_{\min} = d_0/64$ and $h_{\max} = d_0/32$. The computed dimensionless droplet diameter $d(t)/d_0$ is presented in Fig. 3(left). Our numerical solutions demonstrate mesh convergence and are in good agreement with the results presented in [10, 26].

Second, we compare the computed behaviour of the Oldroyd-B fluid with published results. The retardation parameter $\beta = 0.1$, the total viscosity is equal to the Newtonian one $\mu_0 = 4\,\text{Pa} \cdot \text{s}$. Therefore, the solvent and polymer viscosities are $\mu_S = \beta\mu_0 = 0.4\,\text{Pa} \cdot \text{s}$ and $\mu_P = (1 - \beta)\mu_0 = 3.6\,\text{Pa} \cdot \text{s}$, respectively. The dimensionless diameter $d(t)/d_0$ (see right plot in Fig. 3) is in a good agreement with the reference results [10, 25, 26].

Tab. 1: Parameters used in the impacting drop problem.

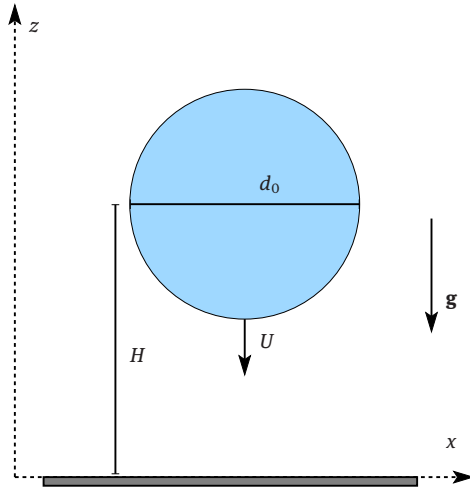| d_0 [m]	H [m]	U [m s^{-1}]	λ_1 [s]	μ_0 [Pa·s]	ρ [kg m^{-3}]	g [m s^{-2}]
0.02	0.04	1.0	0.02	4.0	1000.0	9.81

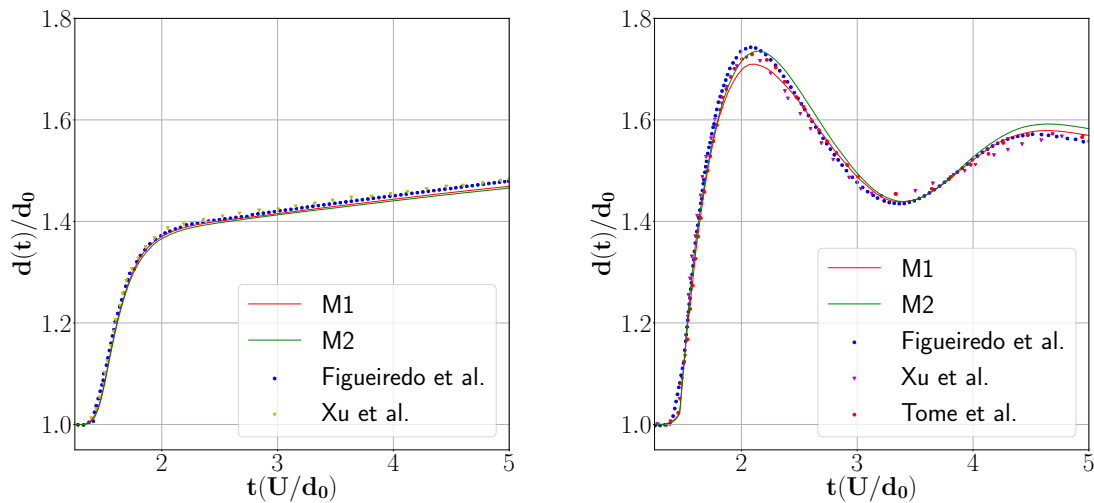**Fig. 2:** Setup for the drop impacting problem.

Fig. 3: Drop diameter over time for viscous fluid (left); viscoelastic fluid with $\beta = 0.1$ (right).

3.2 Oscillating droplet

Oscillations of a free ($\mathbf{g} = 0$) droplet of the viscoplastic or viscoelastic fluid are driven by the surface tension forces and inertia as well as elastic forces for the viscoelastic case.

At the beginning of the simulation the fluid is at rest and the shape of the droplet is a perturbation of a sphere. In spherical coordinates (r, ϑ, φ) the initial shape is given by

$$r = r_0 \left(1 + \tilde{\varepsilon} S_2 \left(\frac{\pi}{2} - \vartheta \right) \right)$$

where S_2 is the second spherical harmonic. The mean surface curvature is not constant, and unbalanced surface tension forces cause droplet oscillations. The presence of fluid viscosity results in the exponential decay of the oscillations due to dissipation.

The computational domain is the cube $(0, l)^3$, $l = 10/3$. The perturbed sphere is placed in the center of the cube. In all experiments we set $r_0 = 1$, the density $\rho = 1$, the surface tension coefficient $\zeta = 1$. The octree grid is dynamically refined from the maximum mesh size $h_{\max} = l/16$ to a mesh size $h_{\min}$ in the vicinity of the
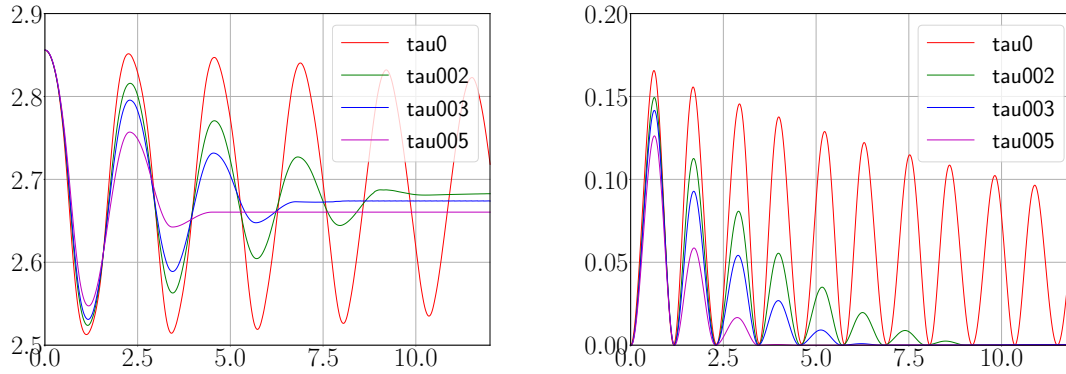
Fig. 4: The viscoplastic droplet top tip z-coordinate (left) and the droplet kinetic energy (right) for the Bingham fluid with yield stress values $\tau_s = \{0, 0.02, 0.03, 0.05\}$.

droplet free surface. The time step is $\Delta t = C\sqrt{\frac{\rho}{2\pi\zeta}}\,h_{min}^{3/2}$, although our implicit method does not impose severe restrictions on the time step.

First, we study the oscillations of the viscoplastic droplet [6, 16]. In the Newtonian regime the oscillation period and the damping factor are of common interest, whereas in the viscoplastic regime one may be interested in the cessation time T_f when the system reaches the arrested state.

We restrict our attention to the yield-stress (Bingham) fluid, which corresponds to the Herschel–Bulkley fluid with the flow index $n = 1$, and study the impact of the yield stress values τ_s to the cessation time T_f.

We set the perturbation amplitude $\tilde{\varepsilon} = 0.3$, the consistency parameter $K = 0.01$ and the minimum mesh size $h_{min} = l/64$.

The computed droplet top tip z-coordinate for different τ_s is shown in Fig. 4(left). The kinetic energy of the droplet is presented in Fig. 4(right). The increase of the yield stress values τ_s causes the decrease of the cessation time T_f.

Second, we study the small-amplitude axisymmetric shape oscillations of the viscoelastic drops [4, 5, 12]. For the Newtonian fluid, the normal-mode analysis predicts the monotonic decrease of the oscillation frequency with the increase of the fluid viscosity. For the Oldroyd-B viscoelastic fluid with the total viscosity $\mu_0 = \mu_S + \mu_P$ (μ_P and μ_S denote polymer and solvent viscosities) this is not always the case: for some combinations of dimensionless parameters, Ohnesorge number $Oh = \mu_0/\sqrt{\zeta\rho r_0}$ and Deborah number $De = \sqrt{8\zeta/(\rho r_0^3)}\,\lambda_1$, the dependence of the oscillation frequency on the total viscosity may become non-monotonic [12]. In particular, according to [5], for $Oh = 0.037$ the frequency increases in the range from $De = 0$ to $De = 1$, and decreases from $De = 1$ till a critical total viscosity value, for which the damping factor causes the initially perturbed surface to return to the spherical form smoothly.

To reproduce this phenomenon, we introduce the dimensionless frequency $Freqless = \sqrt{\rho r_0^3/\zeta}\,\omega$ and the dimensionless damping rate $Dampingless = \sqrt{\rho r_0^3/\zeta}\,d$, where d is obtained by fitting an exponential function e^{-dt} to maximum values of the droplet top tip z-coordinate over periods, and ω is derived from the first oscillation period $\omega = 2\pi/T_1$.

Figure 5 shows the droplet top tip z-coordinate for different De numbers and fixed total viscosity $\mu_0 = 0.01$ and Ohnesorge number $Oh = 0.037$, whereas Figure 6 compares the computed dimensionless frequency and damping rate with published analogues (see [5]). The perturbation amplitude for this experiment is $\tilde{\varepsilon} = 0.1$. Our numerical model is able to catch the non-monotonic frequency behaviour of the Oldroyd-B fluid, the computed $Freqless$ and $Dampingless$ are close to the estimates of the linear asymptotic analysis and the reference values from [5].
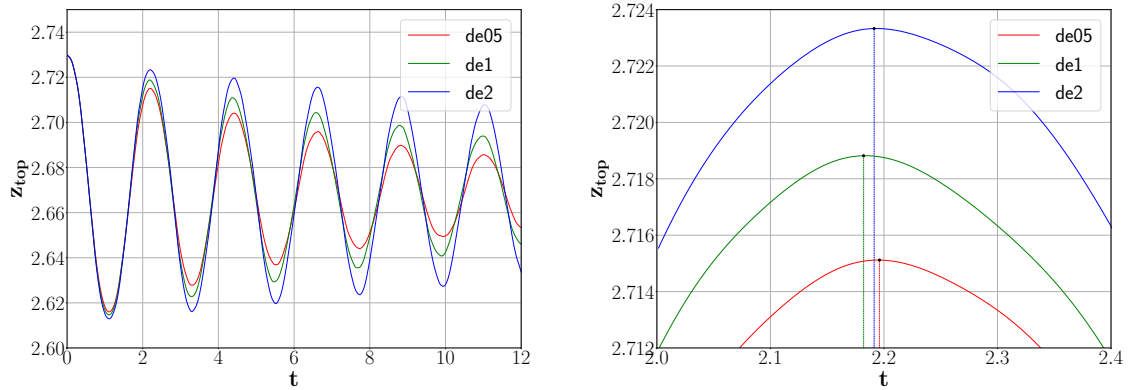
Fig. 5: The viscoelastic droplet top tip z-coordinate (left) with the focus on the first peak (right): De = 0.5 (red), De = 1 (green), De = 2 (blue).
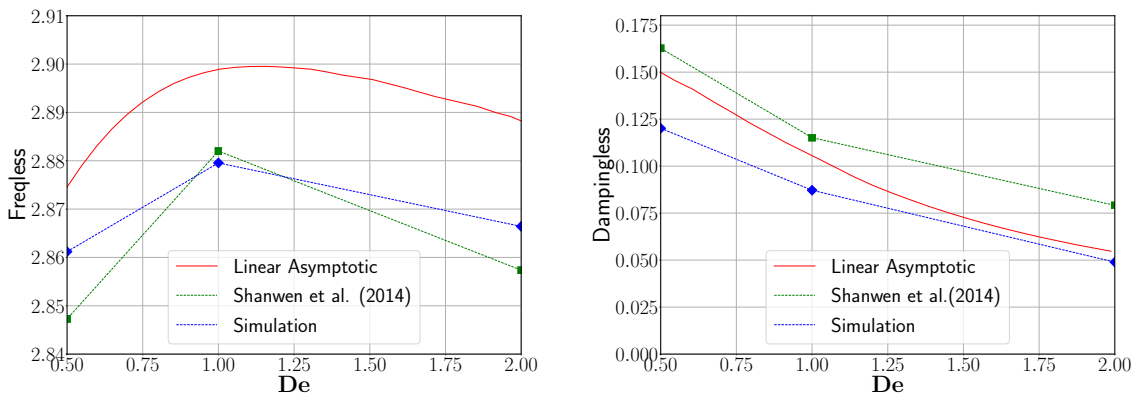

Fig. 6: Dimensionless frequency (left) and damping rate (right) for the viscoelastic droplet: linear analysis (red) and numerical model (green) from [5] versus numerical results in this work (blue).

3.3 Viscoplastic fluid dam break

The last benchmark is based on a physical experiment [7]. A rectangular reservoir is filled with Carbopol Ultrez 10 gel of 0.40% concentration and placed on an inclined plane. The reservoir is equipped with a gate which is perpendicular to the inclined plane. Gate opening releases the fluid which starts to move driven by the gravity force.

Parameters of our simulation correspond to the experimental setting [7]: the reservoir has length $X = 0.51$ m, width $Y = 0.3$ m, and mean height $Z_0 = 0.3$ m. Herschel–Bulkley model parameters K=75.84 Pa $\cdot$ s^{-n}, $n = 0.579, \tau_s = 109$ Pa are shown to approximate [7] the rheology of Carbopol Ultrez 10 gel used in the experiment. The fluid density $\rho = 936.8$ kg/m^3 is chosen to match the known weight 43 kg of fluid filling the reservoir.

In the physical experiment the gate was raised within 0.8 s. We model the fluid motion assuming that the gate is raised gradually within this time. Figure 7 (top) presents the comparison of the simulation and the experimental data for the inclination angle 12°, and Figure 7 (bottom) shows the computed flow depth for different time moments.

The simulation demonstrates that initially the fluid attains fast motion and then decelerates around $t = 2.0$ s. Further, the fluid front evolves gradually and slowly. Such two-stage behaviour of the numerical solution corresponds to the experimental observations, however, the numerical front propagation speed at
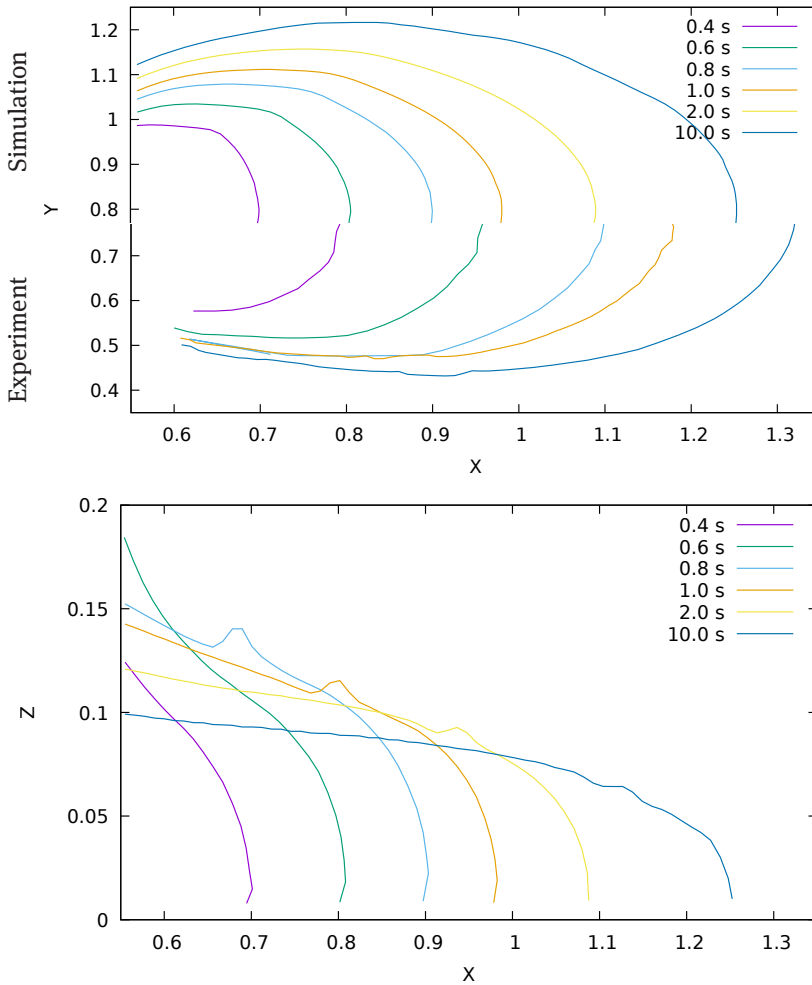
Fig. 7: Top: contact line for simulation (upper half) and experiment [7] (lower half), bottom: flow depth of the viscoplastic fluid.

the first stage is smaller, and the numerical front approaches the experimental one only at $t = 10\,\text{s}$. The mismatch may be explained by inappropriate regime of the gate opening within the simulation and rough approximation of the ground truth rheology by the viscoplastic rheology. Yet the two-stage regime of the flow is recovered correctly.

4 Conclusion

We presented the implicit scheme for simulation of free surface non-Newtonian fluid flows on dynamically adapted octree grids. We addressed two popular fluid models, the viscoplastic Herschel–Bulkley and viscoelastic Oldroyd-B models. The numerical models were verified by comparing the simulations with experimental and numerical results known from the literature.

References

[1] M. A. Alves, F. T. Pinho, and P. J. Oliveira, The flow of viscoelastic fluids past a cylinder: finite-volume high-resolution methods. *J. Non-Newtonian Fluid Mechanics* **97** (2001), No. 2-3, 207–232.

[2] M. A. Alves, P. J. Oliveira, and F. T. Pinho, Benchmark solutions for the flow of Oldroyd-B and PTT fluids in planar contractions. *J. Non-Newtonian Fluid Mechanics* **110** (2003), No. 1, 45–75.

[3] M. Bercovier and M. Engelman, A finite-element method for incompressible non-Newtonian flows. *J. Computational Physics* **36** (1980), No. 3, 313–326.

[4] G. Brenn and S. Teichtmeister, Linear shape oscillations and polymeric time scales of viscoelastic drops. *J. Fluid Mechanics* **733** (2013), 504.

[5] T. Shanwen and G. Brenn, Numerical study for shape oscillation of free viscoelastic drop using the arbitrary Lagrangian-Eulerian method. In: *Int. Conf. on Applied Mechanics and Mechanical Engineering*. **16** (2014), 1–21.

[6] W. Cheng and M. A. Olshanskii, Finite stopping times for freely oscillating drop of a yield stress fluid. *J. Non-Newtonian Fluid Mechanics* **239** (2017), 73–84.

[7] S. Cochard and C. Ancey, Experimental investigation of the spreading of viscoplastic fluids on inclined planes. *J. Non-Newtonian Fluid Mechanics* **158** (2009), No. 1-3, 73–84.

[8] P. Coussot, *Mudflow Rheology and Dynamics*. Routledge, 2017.

[9] M. M. Denn, Issues in viscoelastic fluid mechanics. *Annual Review of Fluid Mechanics* **22** (1990), No. 1, 13–32.

[10] R. A. Figueiredo, C. M. Oishi, J. A. Cuminato, J. C. Azevedo, A. M. Afonso, and M. A. Alves, Numerical investigation of three dimensional viscoelastic free surface flows: impacting drop problem. In: *Proc. of 6th European conference on computational fluid dynamics (ECFD VI)*. **5** (2014), 5368–5380.

[11] R. W. Griffiths, The dynamics of lava flows. *Annual Review of Fluid Mechanics* **32** (2000), No. 1, 477–518.

[12] D. B. Khismatullin and A. Nadim, Shape oscillations of a viscoelastic drop. *Physical Review E* **63** (2001), No. 6, 061508.

[13] Y. Liang, A. Oztekin, and S. Neti, Dynamics of viscoelastic jets of polymeric liquid extrudate. *J. Non-Newtonian Fluid Mechanics* **81** (1999), No. 1-2, 105–132.

[14] B. Meulenbroek, C. Storm, V. Bertola, C. Wagner, D. Bonn, and W. van Saarloos, Intrinsic route to melt fracture in polymer extrusion: a weakly nonlinear subcritical instability of viscoelastic Poiseuille flow. *Physical Review Letters* **90** (2003), No. 2, 024502.

[15] G. Mompean and M. Deville, Unsteady finite volume simulation of Oldroyd-B fluid through a three-dimensional planar contraction. *J. Non-Newtonian Fluid Mechanics* **72** (1997), No. 2-3, 253–279.

[16] K. D. Nikitin, M. A. Olshanskii, K. M. Terekhov, and Yu. V. Vassilevski, A numerical method for the simulation of free surface flows of viscoplastic fluid in 3D. *J. Computational Mathematics* **29** (2011), No. 6, 605–622.

[17] K. D. Nikitin, M. A. Olshanskii, K. M. Terekhov, and Yu. V. Vassilevski, A splitting method for numerical simulation of free surface flows of incompressible fluids with surface tension. *Computational Methods in Applied Mathematics* **15** (2015), No. 1, 59–77.

[18] K. D. Nikitin, M. A. Olshanskii, K. M. Terekhov, Yu. V. Vassilevski, and R. M. Yanbarisov, An adaptive numerical method for free surface flows passing rigidly mounted obstacles. *Computers & Fluids* **148** (2017), 56–68.

[19] K. D. Nikitin, M. A. Olshanskii, K. M. Terekhov, and Yu. V. Vassilevski, A splitting method for free surface flows over partially submerged obstacles. *Russ. J. Numer. Anal. Math. Modelling* **33** (2018), No. 2, 95–110.

[20] M. A. Olshanskii, K. M. Terekhov, and Yu. V. Vassilevski, An octree-based solver for the incompressible Navier–Stokes equations with enhanced stability and low dissipation. *Computers & Fluids* **84** 2013), 231–246.

[21] S. Osher and R. Fedkiw, *Level Set Methods and Dynamic Implicit Surfaces, Vol. 153*. Springer Science & Business Media, 2006.

[22] R. I. Tanner, A theory of die-swell revisited. *J. Non-Newtonian Fluid Mechanics* **129** (2005), No. 2, 85–87.

[23] K. M. Terekhov, K. D. Nikitin, M. A. Olshanskii, and Yu. V. Vassilevski, A semi-Lagrangian method on dynamically adapted octree meshes. *Russ. J. Numer. Anal. Math. Modelling* **30** (2015), No. 6, 363–380.

[24] M. F. Tomé, N. Mangiavacchi, J. A. Cuminato, A. Castelo, and S. McKee, A finite difference technique for simulating unsteady viscoelastic free surface flows. *J. Non-Newtonian Fluid Mechanics* **106** (2002), No. 2-3, 61–106.

[25] C. Viezel, M. F. Tomé, F. T. Pinho, and S. McKee, An Oldroyd-B solver for vanishingly small values of the viscosity ratio: Application to unsteady free surface flows. *J. Non-Newtonian Fluid Mechanics* **285** (2020), 104338.

[26] X. Xu, J. Ouyang, T. Jiang, and Q. Li, Numerical simulation of 3D-unsteady viscoelastic free surface flows by improved smoothed particle hydrodynamics method. *J. Non-Newtonian Fluid Mechanics* **177** (2012), 109–120.